nature communications

Article

https://doi.org/10.1038/s41467-024-51976-5

Engineering active and robust alloy-based electrocatalyst by rapid Joule-heating toward ampere-level hydrogen evolution

Received: 21 March 2024

Accepted: 20 August 2024

Published online: 29 August 2024

Check for updates

Zhan Zhao[1], Jianpeng Sun[1], Xiang Li[1], Shiyu Qin[1], Chunhu Li[1], Zisheng Zhang[2], Zizhen Li[1] & Xiangchao Meng[1]

Rational design of bimetallic alloy is an effective way to improve the electrocatalytic activity and stability of Mo-based cathode for ampere-level hydrogen evolution. However, it is still critical to realise desirable syntheses due to the wide reduction potentials between different metal elements and uncontrollable nucleation processes. Herein, we propose a rapid Joule heating method to effectively load RuMo alloy onto MoOx matrix. As-prepared catalyst exhibits excellent stability (2000 h @ 1000 mA cm^{-2}) and ultralow overpotential (9 mV, 18 mV and 15 mV in 1 M KOH, 1 M PBS, 0.5 M H_2SO_4 solution, respectively) at 10 mA cm^{-2}. Based on first-principle simulations and operando measurements, the impressive electrocatalytic stability and activity are investigated. And the role of rapid Joule heating method is highlighted and discussed in details. This study showcases rapid Joule heating as a feasible strategy to construct highly efficient alloy-based electrocatalysts.

Electrocatalytic splitting of water to produce hydrogen (H_2) has attracted widespread interest[1]. Such carbon-free strategy served as a promising route for addressing ever-increasing environmental issues and the problem of fossil fuels depletion[2]. However, high production cost (ca. US$5 per kg_{H2}) for electrocatalytic hydrogen evolution reaction (HER) restricted its widespread utilization and reduced the economic competitiveness compared with traditional steam methane reforming process (ca. US$2.5 per kg_{H2})[3]. Thus, overcoming the efficiency/stability trade-off for electrocatalytic cathode has been regarded as the mostly feasible approach to improve the economic competitiveness.

For decades, Pt-based catalysts (e.g., commercial Pt/C) have been commercially applied. However, the low reserves and high cost (Pt/C: ~9100 US$ m^{-2}) limited its large-scale deployment in water electrolysis. Molybdenum (Mo)-based electrocatalysts for HER have been comprehensively explored due to its abundant reserves, flexible chemical and electronic structures[4,5]. HER performance of Mo-based electrocatalysts has been effectively improved by various strategies such as phase modulation[6], doping[7], morphology engineering[8] etc. Nevertheless, continuous operation at high current densities using Mo-based catalysts still faced issues of insufficient durability. The harsh operational condition (strong alkaline/acidic electrolyte, high electrode potential, etc.) in practice inevitably caused over-oxidation of Mo to high valence Mo^{n+} ($n > 4$) species (e.g., MoO_4^{2-})[9] and leaching of reactive Mo species, which deteriorated the catalytic activity of Mo-based electrocatalysts[10]. Therefore, it was both attractive and yet challenging to explore suitable strategies for highly reactive Mo-based catalysts in HER while simultaneously achieving long-term stability.

Recently, bimetallic interaction has been proposed to balance the adsorption/desorption free energies between the intermediate and active sites by introducing a suitable second metal with strong *d-d* orbital hybridization to modulate the *d*-band center and charge redistribution of the host metal[11]. Meanwhile, adjacent dual active sites played an important role in overcoming the energy barrier of HER, especially the Volmer process in alkaline solution ($H_2O \rightarrow H^* + OH^*$)[2]. Consequently, bimetallic alloy endowed better activity than those of individual metal catalysts. For instance, Wu et al. proposed heteroatom-tuned strategy and innovatively alloyed Bi metal with Ru

[1]Key Laboratory of Marine Chemistry Theory and Technology (Ministry of Education), College of Chemistry & Chemical Engineering, Ocean University of China, Qingdao, Shandong, China. [2]Department of Chemical and Biological Engineering, Faculty of Engineering, University of Ottawa, Ottawa, ON, Canada. e-mail: mengxiangchao@ouc.edu.cn

nanoparticle to effectively manipulate the charge redistribution of Ru, thus weakening hydrogen-adsorption and achieving 65,000 mA mg^{-1} at 150 mV[12]. Yu et al. found that the negatively shifted *d*-band center of Pt 5*d* orbital in Pt-Fe nanoalloy significantly contributed to reduced adsorption energy of H intermediates[13], and the Pt-Fe sites exhibited co-adsorption effect to promote the H_2O dissociation process. On the other hand, appropriate bimetallic interaction presented exceptionally negative *Ea* to resist the dealloying process in HER[14] and the strong metal-metal interaction could be derived from approximately dull bonding states and empty anti-bonding states, which endowed catalyst desirable stability[15]. Recently, Huang et al. utilized strong *p-d* hybridization interaction among PtGa ultrathin alloy to form electron-rich Pt sites and thus rising reduction potential, which showed excellent durability in 30,000 cycling tests[10].

In this regard, alloying Mo with suitable metal might generate unprecedented HER performance, which not only strengthened stabilization of Mo among lattice atoms in terms of thermodynamics[10] thus inhibiting oxidative release and direct demetallation of Mo, but also accelerated the efficiency of water splitting through the synergistic effect[16]. As the lowest cost precious metal, ruthenium (Ru) was characterized with high intrinsic activity and appropriate proton adsorption energy (ca. 65 kcal mol^{-1})[17–19], and recent studies have demonstrated the synergistic effect between Ru and Mo species according to Brewer-Engel theory[17,20]. However, the wide reduction potentials between different metallic elements[21] and uncontrollable nucleation processes hindered the synthesis of nanoalloy. In general, high temperature (>1300 K) was required to provide activation energy for the formation of atomically dispersed alloy[22]. Meanwhile, another issue associated with well-distributed nanoalloy was thermodynamically driven aggregation, thus a rapid heating/cooling rate was also important. In this context, exploring RuMo alloy-based catalysts with high activity/stability by suitable methods was desirable. Recently, the rapid Joule heating method has been applied as an approach to effectively achieving ultra-high temperatures in a short period[23], realizing mutual solubility of target metals[5]. With the features of generated local high temperature by electricity, multi-metal precursors could be rapidly decomposed and interacted to form ultrafine nanoalloy particles, which accompanied with structural distortion and uncoordinated active sites[24]. Therefore, the rapid Joule heating method may provide a feasible approach to synthesize highly reactive and stable RuMo alloy[25].

In this contribution, we reported a rapid Joule heating method for the synthesis of RuMo nano-alloys (NAs) embedded on MoOx matrix (denoted as RuMo@MoOx-JH) as highly active and robust cathode by replacing the traditional temperature-programmed method. The significant role of Ru alloying in Mo nanoparticles was impressive, wherein synthesized RuMo@MoOx-JH catalyst exhibited an excellent pH-universal activity and stability. Such enhanced activity/stability mechanism was revealed in electronic structure and catalyst-electrolyte interactions level. Meanwhile, experimental and DFT results confirmed the significant role of rapid Joule heating in terms of activity of RuMo@MoOx-JH. Finally, an AEM water electrolyzer assembled with RuMo@MoOx-JH electrode, could deliver 300 mA cm^{-2} with an electricity consumption of 3.82 kW h m^{-3} and an electricity-to-hydrogen energy conversion efficiency of 89.2% at 60 °C, showing competitive cost-effectiveness for industrial applications.

Results and discussion

Joule heating synthesis of RuMo@MoOx-JH catalyst

The synthesis of RuMo@MoOx-JH catalyst by a two-step Joule heating method was shown in Fig. 1a. In brief, three-dimensional flower-like MoO_3 (Supplementary Fig. 1a, b) with a diameter of 5 μm was uniformly grown on pretreated nickel foam (NF) (details in the Experimental Section), followed by rapid self-heating/cooling at 973.15 K for 60 s (Supplementary Figs. 2–6) in the mixed atmosphere of H_2/ Ar (V_1/V_2 = 1:9) to obtain Mo@MoOx-JH on NF. Figure 1b displayed the device for Joule heating process. In detail, the sample was integrated with a carbon paper, which formed conductive pathway and was instantaneously initiated for target temperature by applied current. During calcination, inner Mo atoms diffused and directly anchored on the formed MoO_2, wherein the Mo^0 bonding to MoO_2 substrate was fabricated by the Joule heating treatment[6]. The inset table of Supplementary Fig. 2 showed that rapid Joule heating resulted in a reduction of pyrolysis time to 60 s, and only consumed 0.04% energy of temperature-programmed (TG) method. Zeta potential value for Mo@MoOx-JH was measured as −8.02 mV (MoO_3: −1.39 mV) (Supplementary Fig. 7), indicating a more negatively charged surface to adsorb cations after Joule heating treatment, which might endow enhanced adsorption behavior. Afterwards, the Mo@MoOx-JH was impregnated in the $RuCl_3$ solution to form Mo-O-Ru precursor, which was further in situ reacted on the Joule heating device by ultrafast thermal shock at around 1300 K to prepare RuMo@MoOx-JH (Supplementary Figs. 8–10). The reductive reaction of Ru species by H_2 in the atmosphere was occurred preferentially due to the relevant low standard molar enthalpies of formation at 298.15 K ($RuCl_3$: −205.0 KJ mol^{-1} vs. MoO_2: −588.9 KJ mol^{-1}). Typically, Ru precursor was reduced to the metallic state while other substrates retained original crystal structure[26–28]. Meanwhile, the ultrafast heating process of 500 ms generated activation energy from disorder to order, thus leading to the formation of RuMo nanoalloy[29]. It should be noted that the Ru-Mo bonding resulted in intense *d-d* hybridization interaction, elevated oxidation resistance of Mo and Mo-O* antibonding energy level, which in turn improved the electrocatalytic performance and would be discussed afterwards[10].

Structural characterizations

The crystal structure of as-prepared RuMo@MoOx-JH was verified by X-ray diffraction (XRD) patterns as shown in Supplementary Fig. 11. In addition to primary peaks of the underlying nickel foam, the XRD patterns of RuMo@MoOx-JH and Mo@MoOx-JH samples displayed a group of characteristic signals corresponding to the (110), (101), (211), (310) and (301) facets of the tetragonal structured MoO_2 phase (JCPDS No. 97-009-9714)[6] at 25.9°, 36.9°, 53.3°, 60.3° and 66.7°, respectively. Compared with the MoO_3 pre-catalyst (Supplementary Fig. 11a), XRD patterns demonstrated the phase transformation for molybdenum oxide during the rapid Joule heating treatment. There were no perceptible diffraction peaks indexing to either Ru, Mo or RuMo alloy, resulting from their ultralow content and well-distribution. For scanning electron microscopy (SEM) images (Fig. 2a, d), the pyrolyzed products remained the three-dimensional flower-shaped structure (3 − 5 μm) with roughened surface, which was attributed to rapid Joule heating treatment. And the corresponding energy dispersive spectrometer (EDS) confirmed the coexistence of Ru, Mo, O with low Ru concentration of ~1.73 at.% on RuMo@MoOx-JH (Supplementary Fig. 12 and Supplementary Table 1), which was consisted with XRD result. According to the high-resolution transmission electron microscopy (HRTEM) (Fig. 2b, c), Mo@MoOx-JH catalyst showed hybrid signals containing tetragonal MoO_2 phase (200) and embedded cubic crystal Mo nanoparticle (NP) (111), which corresponded to the measured lattice spacings of 2.42 Å and 2.30 Å, respectively. Moreover, the size of NP was measured to be ~3 nm, which effectively, via Joule heating, avoided agglomeration and consequential catalyst deactivation[30]. It was noted that the introduction of Ru species resulted in the formation of RuMo nanoalloy (NA), wherein the lattice spacings indexed to Mo_2Ru (150) and MoO_2 (200) facets could be clearly detected (Fig. 2e, f). And the atomic-resolution HAADF-STEM image was performed to verify the Ru atom in Supplementary Fig. 13. Besides, the energy-dispersive X-ray spectroscopy (EDX) elemental mapping of RuMo NA in Supplementary Fig. 14, 15 indicated the homogeneous distribution of Ru and Mo elements. The well-distributed RuMo NAs

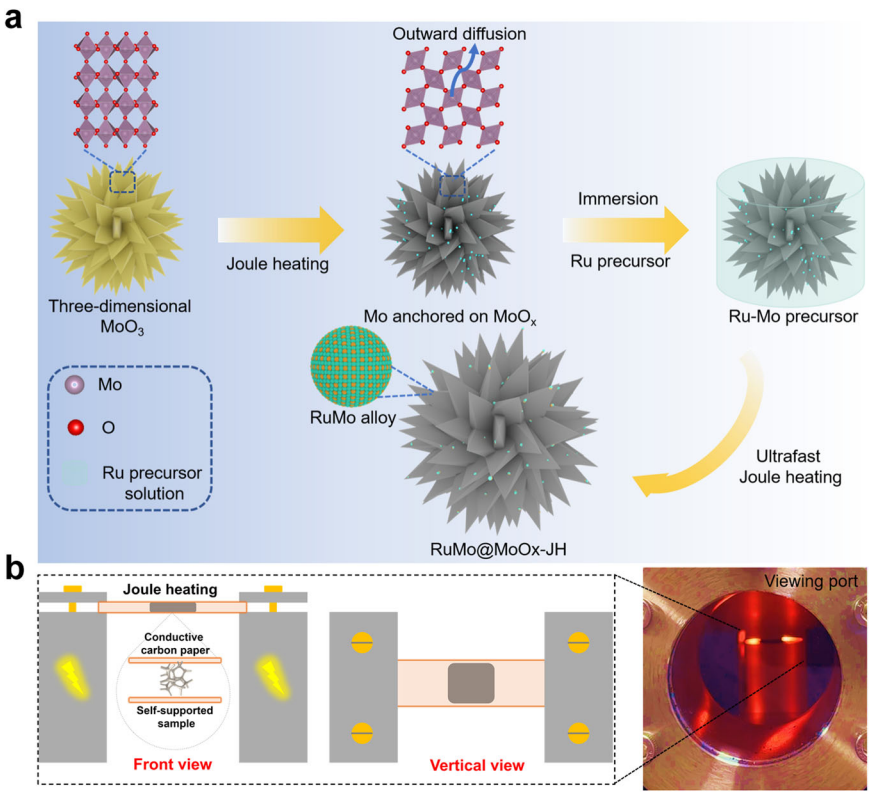

Fig. 1 | Synthesis of RuMo@MoOx-JH catalyst by Joule heating method. a Schematic illustration of the synthesis of RuMo@MoOx-JH catalyst by the rapid Joule heating method. **b** Schematic diagram of the working condition of Joule heating device (left) and the optical picture of catalyst on NF at high temperature (right).

could be observed on the TEM images (Supplementary Fig. 16), which was consisted with XRD results. In details, the RuMo NAs with small average size of about 3.17 nm were uniformly on the MoOx in the TEM image of RuMo@MoOx-JH. HRTEM result further confirmed that Ru and Mo signals were atomic distributed through RuMo NA, which consisted of the (150) crystalline plane of Mo_2Ru. For further verification of RuMo NAs, the line scan measurement using energy-dispersive X-ray spectroscopy was applied to demonstrate that Ru and Mo elements were well-distributed throughout NA (Fig. 2g, h). During the formation of RuMo NA, the ultrafast Joule heating caused thermo-migration and fluctuation of Ru/Mo atoms[31], leading to lattice compressive strain and transient dislocations, which could be significantly remained due to the rapid cooling rate (361 K/s) (Supplementary Fig. 10). As expected, Fig. 2f exhibited rich lattice dislocations in MoO_2 crystal structure among RuMo@MoOx-JH. Meanwhile, the geometric phase analysis (GPA) was performed for the RuMo NA, wherein ε_{xx} component of strain tensor revealed significant strain impact (Fig. 2i). To bolster this assertion, geometric phase analysis on Mo@MoOx-JH was conducted to reveal the role of rapid quenching in the joule heating process (Supplementary Fig. 17), wherein strain tensor was also detected on Mo NP. Additionally, an augmented presence of strain was effectively showcased through the strain distributions of Mo NP and RuMo NA, which indicated the positive influence of thermal shock with high temperature in producing rich dislocation[32]. Of note, such generated lattice disorder could serve as active sites and was beneficial for hydrogen adsorption[33].

X-ray photoelectron spectroscopy (XPS) was employed to gain insight into the electronic characteristics. As shown in Fig. 3a, Mo $3d_{5/2}$ and $3d_{3/2}$ peaks located at 238 eV to 228 eV for both samples implied the presence of Mo with a valence state of δ ($0 \le \delta \le 6$) after deconvolution. Typically, the Mo^0 signals (228.4 eV for Mo^0 $3d_{5/2}$ and 231.5 eV for Mo^0 $3d_{3/2}$) at low binding energy could be observed indicating the metallic Mo states among RuMo NAs and Mo NPs[34]. In particular, the in situ synthesis of Mo@MoOx-JH and RuMo@MoOx-JH via Joule heating process induced reduction of Mo species, as evidenced by the relatively low valence of Mo compared to bare MoO_3 (Supplementary Fig. 18a). Such phase transition was characterized with higher conductivity of MoO_2, which was caused by modified electrons in Mo-O bonds ($t_{2g}^2 e_g^0$ for Mo species)[35]. In addition, the core-level Ru 3*p* spectra could be deconvoluted into two states of Ru (Fig. 3b), wherein the dominant peaks of 462.3 eV and 484.6 eV belonged to metallic Ru. Other peaks with trace amount was from Ru^{4+} (Ru^{4+}: Ru^0 = 0.15: 1), manifesting Ru precursor was successfully transferred to RuMo NAs with Mo species[36]. The O 1*s* XPS spectrum peaks at 530.6 eV, 531.9 eV and 533.3 eV were characteristics of the formation of lattice oxygen (O_L), oxygen vacancy (O_V) and oxygen from adsorbed water (O_{H2O}) (Fig. 3c). The rich Ov might be caused by the Joule heating among reductive atmosphere[34], as revealed by O 1*s* XPS spectrum for MoO_3 (Supplementary Fig. 18b). Furthermore, to investigate the atomic coordination environment and valance state of RuMo@MoOx-JH, the Ru K-edge X-ray absorption spectroscopy (XAFS) spectra was utilized with Ru foil and RuO_2 standards. The pre-edge of X-ray absorption near-edge structure (XANE) region revealed that the valence energy of Ru atoms in RuMo NAs was much lower than that of RuO_2 (+4) but resembled that of Ru foil (0) demonstrating metallic nature of the Ru (Fig. 3d), consistent with the XPS result (Fig. 3b). The slightly oxidized state might be caused by under-coordinated edge and corner Ru atoms among NAs[37], which played an important role in tuning catalyst-H interaction and consisted with GPA results in Fig. 2i. Meanwhile, the electronic transition between Ru and Mo could be reflected by the much higher simultaneous line intensity of the K-edge XANES spectrum than Ru foil[38]. As shown in the Fourier transform extended X-ray absorption fine structure (FT-EXAFS) spectra (Fig. 3e), two predominant peaks could be detected, wherein the slight broad peak at ~1.53 Å originated from Ru-O scattering owing to minor oxidization. Other peak (~2.42 Å) confirmed the strong Ru-Mo interaction.

https://doi.org/10.1038/s41467-024-51976-5

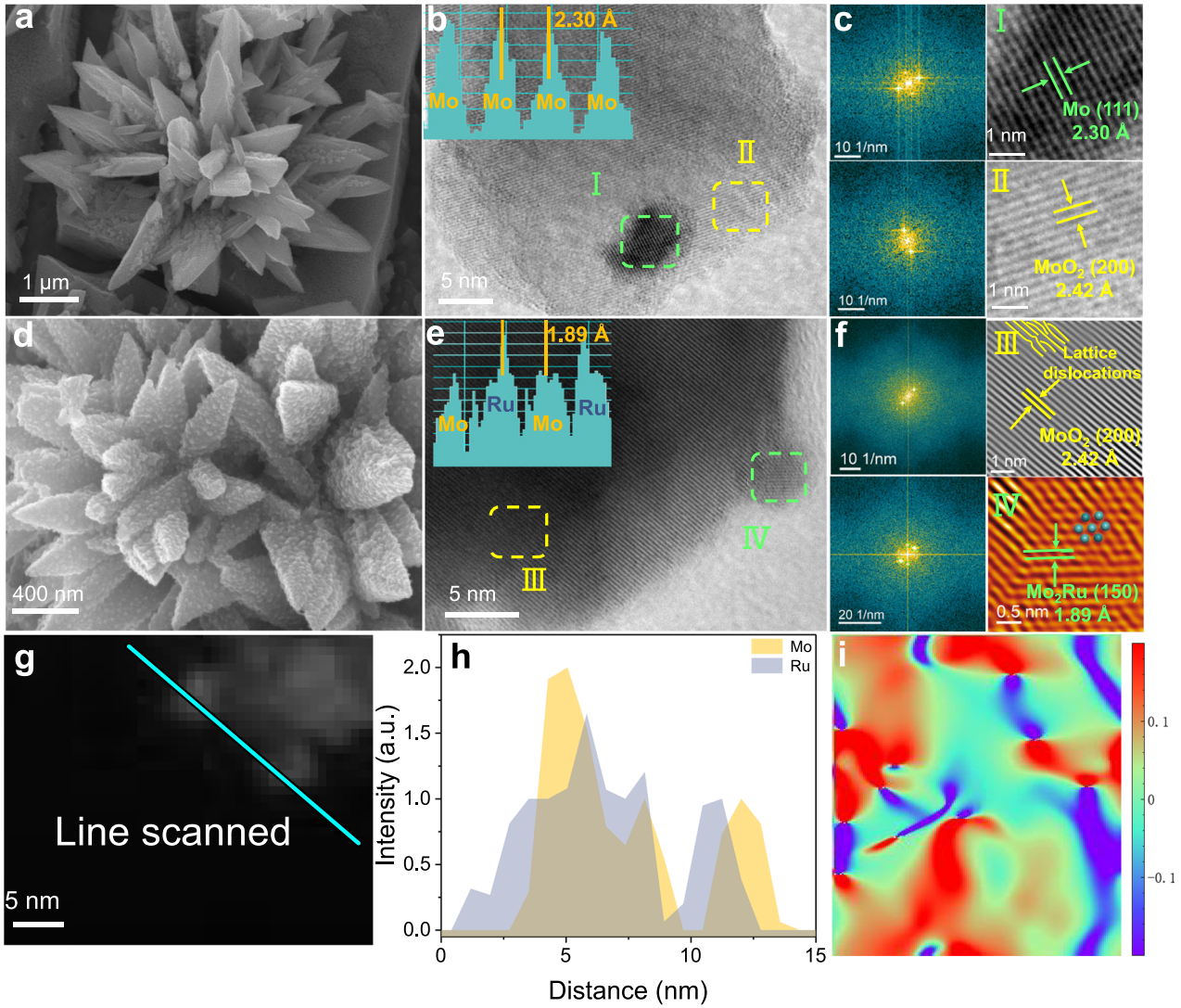

Fig. 2 | The component and structure of Mo@MoOx-JH counterpart and RuMo@MoOx-JH. a SEM image of Mo@MoOx-JH. **b**, **c** TEM image of Mo@MoOx-JH. **d** SEM image of RuMo@MoOx-JH. **e**, **f** TEM image of RuMo@MoOx-JH. **g** Line scanned image for RuMo NA. **h** Elements distribution derived from line scanned image. **i** Strain distributions of εxx for RuMo@MoOx-JH. Source data for Fig. 2 are provided as a Source Data file.

Obviously, the coordination element in RuMo NAs was different from contrasted samples. Correspondingly, the non-detectable Ru-Ru scattering (~2.38 Å) in RuMo NAs could further give additional information on Ru-Mo coordination environment, wherein the marginally more positive peak might be the formation of RuMo NAs[17]. And this was believed that the elongated Ru-Mo bond length demonstrated the formation of RuMo alloy[17]. The significantly reduced intensity of peak (~2.42 Å) for RuMo@MoOx-JH was ostensibly caused by the incorporation of Ru atoms around Mo atoms[39]. In addition, from the viewpoint of EXAFS oscillation functions of RuMo@MoOx-JH in Fig. 3f, smaller amplitudes than that of Ru foil could be assigned to the finite size effect of RuMo NAs (~5 nm) and was consistent with TEM[40]. For obtaining detailed coordination numbers (CN) and configuration of Ru species among RuMo@MoOx-JH, the EXAFS fitting was investigated, when applicable (Supplementary Fig. 19 and Supplementary Table 2). The Ru-Mo coordination environment were identified based on the Mo_2Ru model, wherein the CN was 7.01 with the Ru-Mo interatomic distance of 2.71 Å, further confirming the formation of RuMo NAs and consistent with TEM results. In line with the FT-EXAFS spectra, wavelet transform (WT) EXAFS contour plot (Fig. 3g) of RuMo@MoOx-JH showed intensity maximum at ~9.98 $Å^{-1}$ for Ru-Mo coordination, which was different from Ru foil (~10.64 $Å^{-1}$) and RuO_2 (~10.75 $Å^{-1}$) for Ru-Ru coordination, suggesting the altered local configuration owing to the formation of RuMo NAs. Therefore, above results demonstrated isolated Ru atoms in Mo matrix with the formation of RuMo NAs.

Evaluation of HER electrocatalysis using RuMo@MoOx-JH catalyst

The conventional three-electrode cell configuration was applied to comprehensively evaluate electrocatalytic activity of RuMo@MoOx-JH in H_2-saturated electrolyte with different pH at 25 °C, wherein the Mo@MoOx-JH, Pt/C (150 $\mu g_{Pt}/cm^{-2}$) and NF were measured for comparison. As shown in Fig. 4a and Supplementary Fig. 20, RuMo@MoOx-JH displayed ultralow overpotential of 9 mV in KOH solution (1 M) to deliver a current density of 10 mA cm^{-2}, which was much lower than that of contrasted sample. Meanwhile, to confirm the optimum content of Ru in RuMo@MoOx-JH, HER activities of samples with different Ru ratios were explored (Supplementary Fig. 21), which were synthesized by increasing the concentration of Ru precursor ($RuCl_3$ solution). Impressively, RuMo@MoOx-JH also exhibited excellent activity at ampere-level current density with an overpotential of 169 mV and 256 mV at 1 A cm^{-2} and 2 A cm^{-2} in KOH solution, which was pretty lower than Pt/C (341 mV @ 1 A cm^{-2}). Comparatively, Mo@MoOx-JH

https://doi.org/10.1038/s41467-024-51976-5

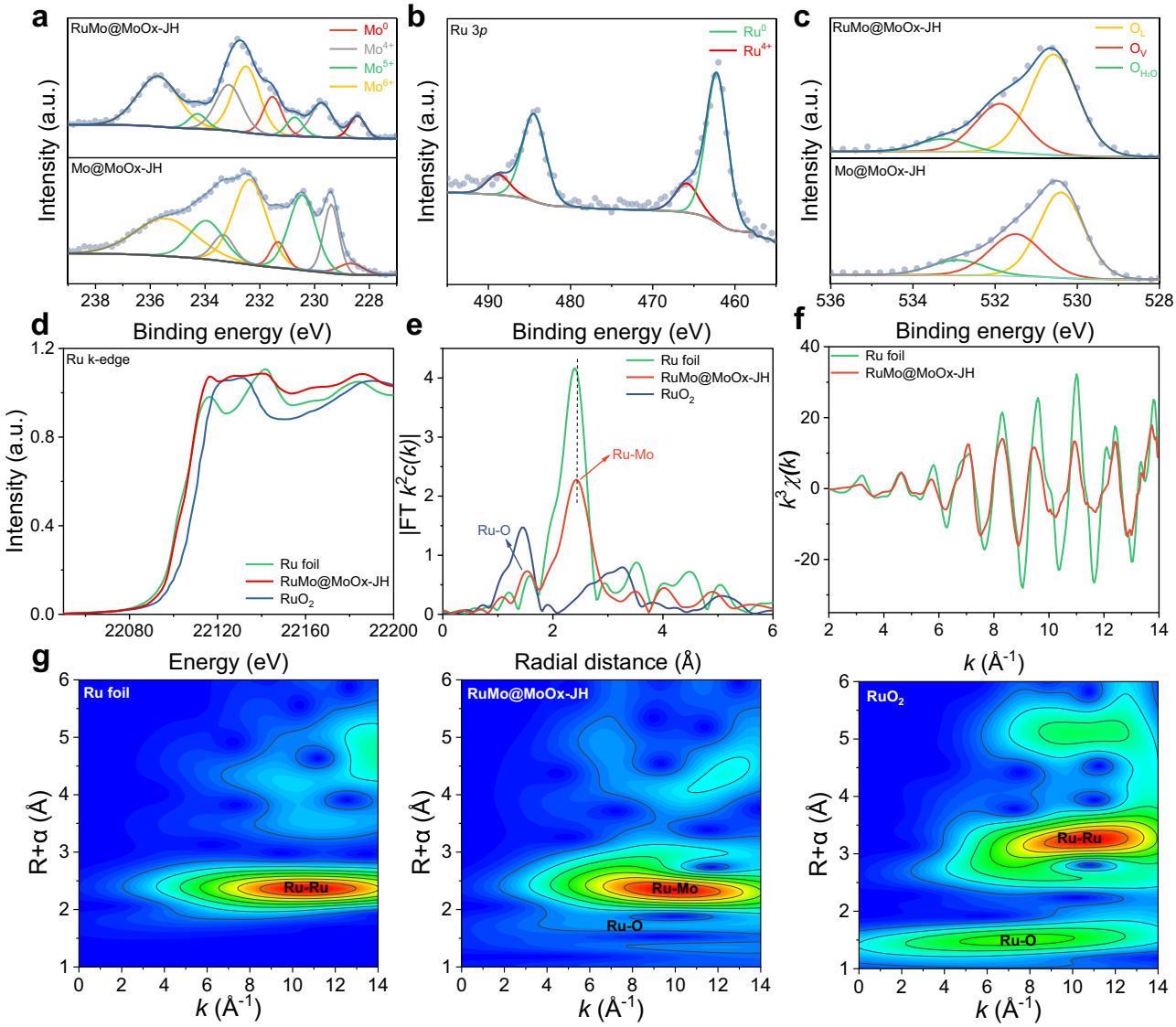

Fig. 3 | Surface chemical state and coordination environment analysis of RuMo@MoOx-JH. a Mo 3*d* XPS spectra of Mo@MoOx-JH and RuMo@MoOx-JH. **b** Ru 3*p* XPS spectra of RuMo@MoOx-JH. **c** O 1*s* XPS spectra of Mo@MoOx-JH and RuMo@MoOx-JH. **d** Ru k-edge synchrotron-based XANES of RuMo@MoOx-JH, Ru foil and RuO_2. **e** FT-EXAFS spectra for the Ru k-edge. **f** EXAFS oscillation functions of RuMo@MoOx-JH and Ru foil. **g** WT-EXAFS curves for Ru foil (left), RuMo@MoOx-JH (middle), and RuO_2 (right). Source data for Fig. 3 are provided as a Source Data file.

showed inferior catalytic performance, achieving 2 A cm^{-2} at 1.59 times overpotential (406 mV) of RuMo@MoOx-JH, which clearly demonstrated the role of incorporation of Ru and the origin of the activity would be discussed below. Meanwhile, Supplementary Fig. 22 displayed the Tafel pots based on the polarization curve data in KOH solution, which were applied to compare the activation energy of the catalysts. Typically, the Tafel slope of RuMo@MoOx-JH was evaluated to be 28.6 mV dec^{-1}, surpassing that of Mo@MoOx-JH (62.4 mV dec^{-1}), Pt/C (77.5 mV dec^{-1}) and NF (251.3 mV dec^{-1}). Additionally, the Tafel slope of RuMo@MoOx-JH revealed fast reaction kinetics, following the Volmer-Tafel mechanism[41]. The double-layer capacitance (C_{dl}) in non-Faradaic voltage window was examined in KOH solution to investigate the intrinsic catalytic activity. As shown in Supplementary Fig. 23, RuMo@MoOx-JH possessed a C_{dl} value of 389.6 mF cm^{-2}, nearly 1.71- and 38.6-fold higher than that of Mo@MoOx-JH (227.5 mF) and NF (10.1 mF) counterparts, respectively. This result revealed the introduction of RuMo NAs provided abundant active sites.

Notably, the pH-universal responded catalysts played an important role when applied in practice[13]. For verification, the electrochemical properties of as-prepared samples were investigated in 1 M PBS and 0.5 M H_2SO_4 electrolyte. As could be seen from Fig. 4b, c and Supplementary Figs. 24, 25, RuMo@MoOx-JH also required a low overpotential of 18 mV and 15 mV to deliver 10 mA cm^{-2} in PBS and H_2SO_4 solution, respectively. Additionally, the Tafel slopes of RuMo@MoOx-JH were evaluated to be 83.5 and 39.9 mV dec^{-1} in neutral and acidic solution, respectively, wherein the small value indicated fast reaction kinetics (Supplementary Fig. 22). Meanwhile, to exclude the excellent performance endowed by possible deposition of Pt element, the XPS spectra of electrode after stability testing and electrochemical analysis were applied (Supplementary Fig. 26), which could be proved by the absence of Pt 4*d* XPS spectra on the RuMo@MoOx-JH. To ensure the reproducibility of results, the *iR*-free HER performance of RuMo@MoOx-JH in different electrolytes were provided in Supplementary Fig. 27. The above results indicated excellent pH-universal HER performance of as-prepared sample. To reveal the HER kinetics of catalysts among high current densities, the $\Delta\eta/\Delta log|j|$ ratios was performed and evaluated in KOH solution (Fig. 4d) (η and j corresponded to overpotential and current density, respectively). In

https://doi.org/10.1038/s41467-024-51976-5

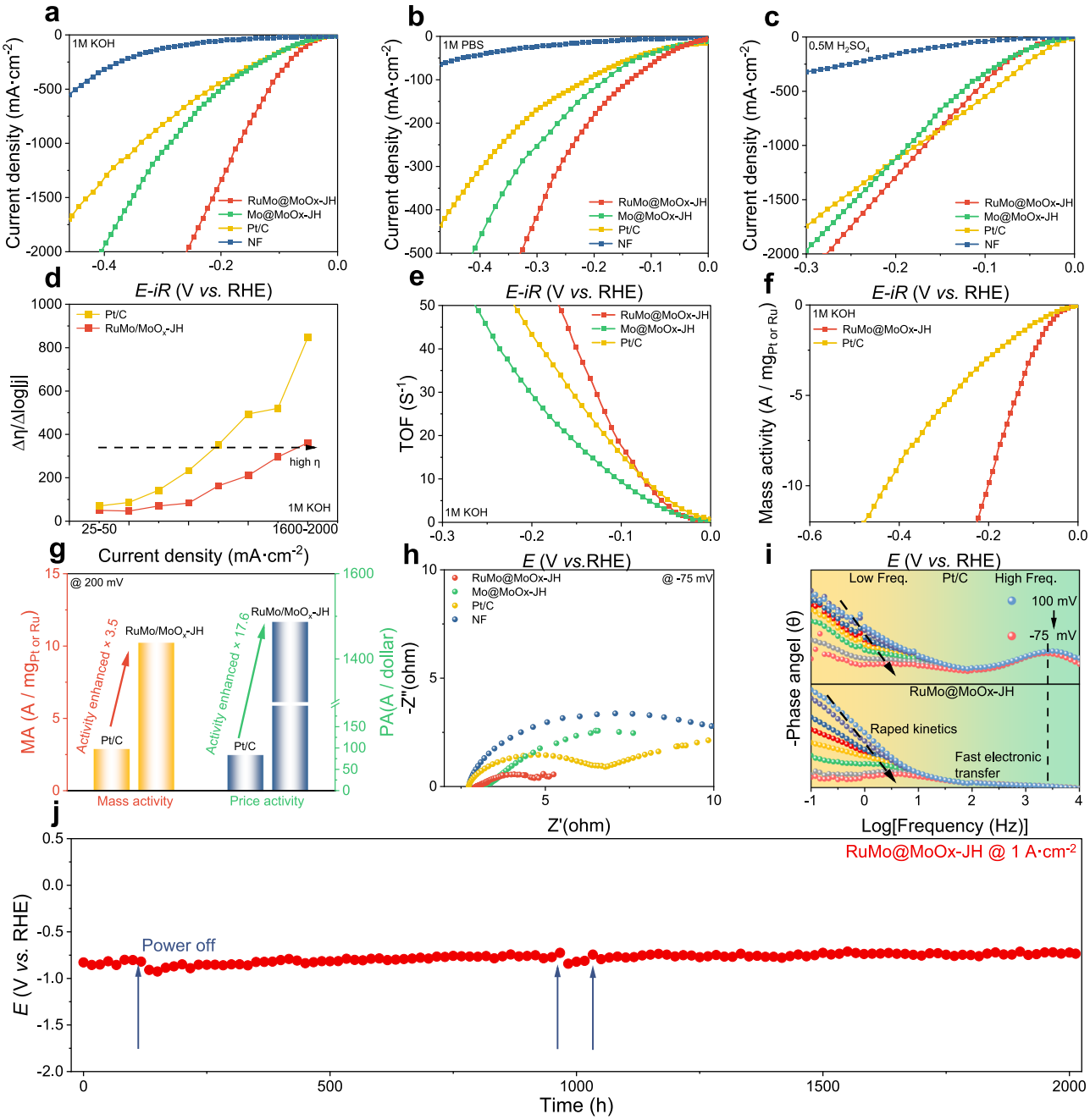

Fig. 4 | Electrocatalytic HER performance test of catalysts. The non-*iR* corrected polarization curves were provided in the Supplementary Information (The electrode surface area was 0.5 cm × 0.4 cm). **a** Polarization curves of RuMo@MoOx-JH with the reference of Mo@MoOx-JH, Pt/C, and NF. The electrolyte was 1 M KOH solution (The measured pH was 13.65 and the resistance was 2.67 ± 0.48 Ω). **b** Polarization curves in 1 M PBS solution (The resistance was 8.82 ± 0.49 Ω). **c** Polarization curves in 0.5 M H_2SO_4 solution (The measured pH was 0.26 and the resistance was 1.85 ± 0.20 Ω). **d** $\Delta\eta/\Delta log|j|$ ratios of RuMo@MoOx-JH and Pt/C in 1 M KOH solution. **e** Potential-dependent turnover frequency (TOF) curves of different electrocatalysts in KOH solution. **f** The mass activity curves for RuMo@MoOx-JH and Pt/C in 1 M KOH solution. **g** The mass activities and calculated price activities for RuMo@MoOx-JH and Pt/C. **h** Nyquist plots measured in1 M KOH solution. **i** The corresponding Bode phase plots for RuMo@MoOx-JH and Pt/C. **j** Chronopotentiometry measurement without *iR*-compensation of RuMo@MoOx-JH at 1 A cm^{-2} for 2000 h. Source data for Fig. 4 are provided as a Source Data file.

detail, the Pt/C electrode possessed increased value of $\Delta\eta/\Delta log|j|$ as the current density range increased to 2000 mA cm^{-2} (Supplementary Table 3), e.g., *j*: 400–800 mA cm^{-2} for $\Delta\eta/\Delta log|j|$: 352.1 mV dec^{-1}, while the RuMo@MoOx-JH remained 162.7 mV dec^{-1} (0.46-fold of Pt/C), suggesting the ultrafast HER kinetics in KOH solution. To elucidate the intrinsic mechanism of the HER activity, the LSV curves of different electrocatalysts were normalized by electrochemical active surface area (ECSA). As shown in Supplementary Fig. 28, RuMo@MoOx-JH possessed the highest current density of 0.21 mA cm^{-2} at η_{200} in 1 M KOH solution, which was 1.11 and 1.62-fold of Pt/C (0.19 mA cm^{-2}) and Mo@MoOx-JH (0.13 mA cm^{-2}), respectively. Moreover, RuMo@MoOx-JH also presented a high current density of 0.04 mA cm^{-2} @ η_{200} and 0.31 mA cm^{-2} @ η_{250} in 1 M PBS and 0.5 M H_2SO_4 solutions (Supplementary Figs. 29 and 30), respectively, validating that RuMo@MoOx-JH owned the highest intrinsic activity besides the largest ECSA. Meanwhile, the turnover frequencies (TOFs) were further calculated to assess the intrinsic activities of RuMo@MoOx-JH (Fig. 4e and Supplementary Fig. 31), which exhibited a high TOF value of 40.5 s^{-1}, 5.8 s^{-1},

and 41.6 s^{-1} at η_{150}, corroborating the excellent intrinsic HER activity in pH-universal electrolytes.

To gain insight into the electrocatalytic activity of electrodes, the platinum group metals (PGM) (Ru or Pt) mass activity was computed (detailed calculation in Supporting Information) (Fig. 4f). The RuMo@MoOx-JH exhibited higher Mass-normalized activity compared with Pt/C electrode (@ 200 mV: 10.2 A mg_{Ru}^{-1} vs 2.9 A mg_{Pt}^{-1}). Meanwhile, considering the various metal prices, the normalized activity derived from price was calculated by dividing the geometric current density by corresponding cost of PGM (Fig. 4g). As expected, the RuMo@MoOx-JH significantly outperformed the Pt/C (@ 200 mV: 1486.9 A $dollar_{Ru}^{-1}$ vs 84.4 A $dollar_{Pt}^{-1}$), which revealed the advance from sustainable point of view. In addition, the electrochemical kinetics was evaluated using electrochemical impedance spectroscopy (EIS) measurements (Fig. 4h and Supplementary Fig. 32), which was evidenced by the lowest charge transfer resistance (R_{ct}) of RuMo@MoOx-JH among all the sample at applied overpotential of −75 mV (Fig. 4h). The Fig. 4i showed the Bode plots in 0.1 V to −0.075 V vs RHE of RuMo@MoOx-JH and Pt/C electrodes, which derived from the *operando* EIS tests. The response of the low-frequency regions was associated with Volmer step in alkaline media ($* + H_2O + e^- \rightarrow H^* + OH^-$, where * was the active sites and H* was the adsorbed hydrogen), as revealed advantageous Volmer process kinetics by the faster decay of phase angle peak for RuMo@MoOx-JH than that of Pt/C. Furthermore, the high-frequency region also suggested that RuMo@MoOx-JH exhibited much higher electron transferability from inner layer to the real active sites than Pt/C, which has cognized as main factor inhibiting the HER process[42]. Besides of excellent electrocatalytic activity, long-term stability was applied under high current density, which was evaluated as significant concern for industrial application (>500 mA cm^{-2})[43]. Thus, as-prepared RuMo@MoOx-JH durability was evaluated by chronopotentiometry test up to constant current density of 1 A cm^{-2}. As could be seen in Fig. 4j, the superior alkaline HER performance was retained even in 2000-h operation without obvious decay, signifying the high stability of RuMo@MoOx-JH for potential industrial application. The XRD, XPS and SEM results confirmed the high chemical stability and structure integrity after long-term electrolysis (Supplementary Figs. 33 and 34).

Mechanism of alloying Ru by Joule heating on the HER catalytic stability and activity

For the comparison of stability, the E-t curves of Mo@MoOx-JH at 200 mA cm^{-2} was shown in Supplementary Fig. 35. It should be noted that the increased potential of Mo@MoOx-JH showed process of significant activity decline (~10 mV within 9 h). Generally, the dissolved Mo species, under large current density, could attributed to the activity decay following previous reports[44,45]. Consequently, to further investigate the mechanism for the excellent stability of RuMo@MoOx-JH, the Inductively coupled plasma-optical emission spectrometer (ICP-OES) measurements were conducted to determine the dissolved Mo content in alkaline HER process, wherein the Mo@MoOx-JH was also evaluated at same condition. For as-synthesized RuMo@MoOx-JH, the low dissolved Mo concentration at 0–3 h range (2.78 mg L^{-1}) manifested effective maintenance of the Mo site (Fig. 5a), which was much lower than Mo@MoOx-JH (5.85 mg L^{-1}: 2.1-folds of RuMo@MoOx-JH). Meanwhile, it was noted that the dissolved Mo concentration remained at 3.57 mg L^{-1} after 9 h continuous electrolysis, while the significant Mo species loss could be observed on Mo@MoOx-JH with the value of 6.23 mg L^{-1}, 7.46 mg L^{-1}, 8.65 mg L^{-1}after 6, 9, 12 h, respectively. This result could also be revealed by the dissolution rate curves in Fig. 5a (0.42 mg L^{-1} h^{-1} vs 0.01 mg L^{-1} h^{-1}). Notably, the rather low concentration (0.056 mg L^{-1}) of dissolved Mo among refreshed KOH solution further highlighted the enhanced structural robustness due to the integration of Ru and Mo, while the same phenomenon could also be observed in acidic solution (Supplementary Fig. 36 and 37). Meanwhile, theoretical calculations were used to elucidate the underlying mechanism of the superior stability of the RuMo@MoOx-JH catalyst (Supplementary Data 1). The vacancy formation energy of Mo could be a decisive factor in the stability at large current density[10,38]. As shown in Fig. 5b, alloying of Ru atoms into Mo was characterized with 9.36 eV, which was much higher than that of Mo NP (7.12 eV), indicating improved antioxidation ability. In addition, the exploration of chemical bond among Mo 3*d* and O 2*p* was determining factor for investigating the stability of regenerated RuMo@MoOx-JH with introduction of Ru atom, wherein *d*-band center theory has been widely used to explain bonding environment for catalyst with *d*-orbital[46]. Supplementary Fig. 38 and Supplementary Data 1

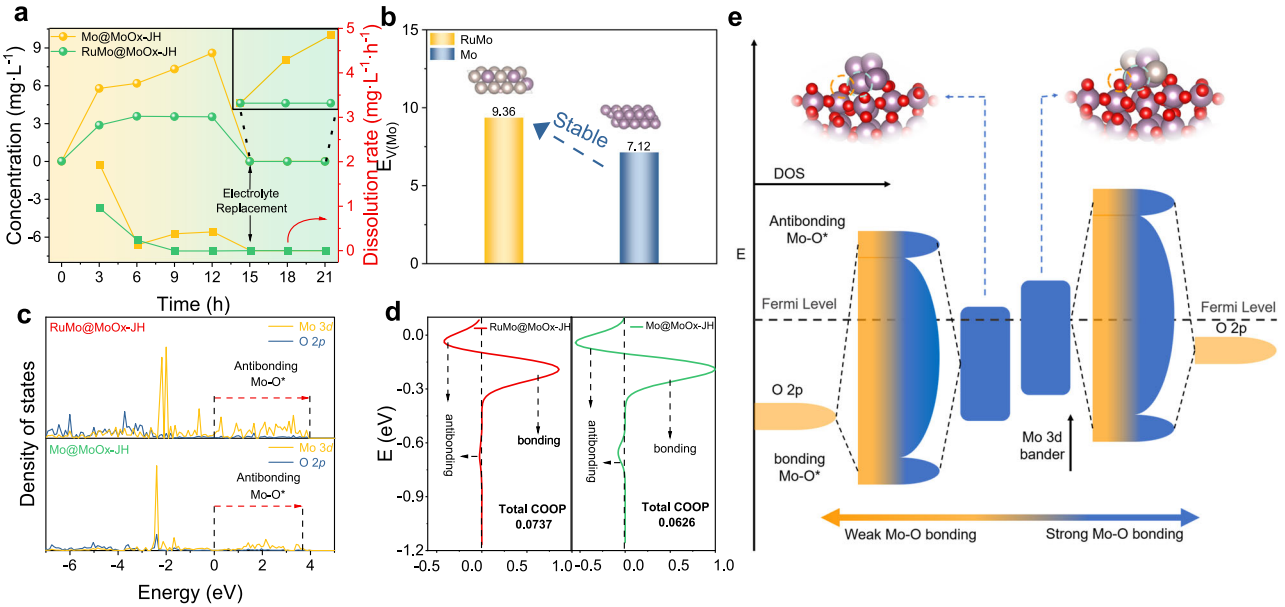

Fig. 5 | Stability mechanism investigation. a ICP-OES of RuMo@MoOx-JH (green) and Mo@MoOx-JH (yellow) at 200 mA cm^{-2} in KOH containing the Mo dissolution concentration (up) and dissolution rate (down). **b** Mo vacancy formation energies ($E_{V(Mo)}$) for Mo and RuMo NA. **c** Mo 3*d* and O 2*p* pDOS of RuMo@MoOx-JH and Mo@MoOx-JH. **d** COOP for the Mo-O bond in RuMo@MoOx-JH and Mo@MoOx-JH. **e** Schematic of the rise of the Mo *d*-band center in RuMo@MoOx-JH and Mo@MoOx-JH. Source data for Fig. 5 are provided as a Source Data file.

illustrated the optimized models of Mo@MoOx-JH and RuMo@MoOx-JH, which provided the basis to the projected density of state (pDOS) analyses (Supplementary Fig. 39). For RuMo@MoOx-JH, it should be noted that the position of Mo's *d*-band center emerged at −0.929 eV, showing a up shift compared with Mo@MoOx-JH (−1.079 eV). Meanwhile, the *d*-*p* interaction between Mo and O could be clearly observed in Fig. 5c. The antibonding Mo-O* orbitals of RuMo@MoOx-JH systems moved slightly away from Fermi level after the introduction of Ru, which indeed rationalized the excellent stability from experimental evidence (1 A cm^{-2} @ 2000 h) (Fig. 4g). Furthermore, crystal orbital overlap population (COOP) was calculated to prove the strength of Mo-O bond among Mo NP-Mo-O-MoO_2 and RuMo NA-Mo-O-MoO_2, respectively. As shown in Fig. 5d, the integrated area of COOP (ICOOP) for Mo-O bond in RuMo@MoOx-JH (0.0737) was higher than that in Mo@MoOx-JH (0.0626), which was directly proportional to occupancy of bonding state after alloying Ru with Mo. Therefore, such results demonstrated the regulation effect of Ru on Mo-O interaction. We reasonably concluded that the Mo's elevated *d*-band center caused by introduction of Ru raised Mo-O* antibonding energy level in RuMo@MoOx-JH, which allowed that electrons of the O 2*p* orbital preferentially flow to bonding Mo-O orbital and effectively restrained Mo migration as depicted in Fig. 5e.

To elucidate the origin of the improved HER catalytic activity by the formation of RuMo NAs, the density functional theory (DFT) calculations were carried out to probe the electronic structure (Supplementary Data 1). As shown in Supplementary Fig. 40a, the RuMo NA system possessed more states around Fermi level than Ru NP and Mo NP, revealing that formation of RuMo NA was beneficial to the electrical conductivity. In addition, the pDOS of *d*-orbitals for RuMo NA and Mo NP were analyzed, wherein the *d*-band center exhibited a shift from −0.791 eV (Mo NP) to −1.414 eV (RuMo NA) upon the introduction of Ru (Supplementary Fig. 40b). From the *d*-band theory, the down shift of *d*-band center could endow the active site weaker binding with adsorbates (H for HER process)[11]. Specifically, the ΔG_{H^*} values were calculated as depicted in Supplementary Fig. 40c. As expected, RuMo NA system (−0.21 eV) showed more negative adsorption reaction than that of Mo NP system (−1.09 eV), indicating the regulated binding to adsorbates, which was consistent with *d*-band center theory (Supplementary Fig. 40d). Meanwhile, the moderate ΔG_{H^*} values of -0.21 eV was associated with rapid HER kinetics, which indeed rationalized more excellent performance of RuMo@MoOx-JH than Mo@MoOx-JH from experimental evidence (Fig. 4a).

For further exploration of the possible catalytic mechanism at macro-scale after the introduction of Ru, we carried out in situ Raman measurement on RuMo@MoOx-JH and Mo@MoOx-JH in 1 M KOH solution to track the HER reaction at surface (Supplementary Fig. 41). As shown in Fig. 6a and d, Raman bands around 236, 373, 414, 642 and 747 cm^{-1} at open circuit voltage (OCV) were clearly observed both in RuMo@MoOx-JH and Mo@MoOx-JH, which was indexed to the characterized peaks of MoO_2[47]. Most importantly, it should be noted that the signal of 1027 cm^{-1} corresponded to adsorbed OH intermediates (*OH) on Mo sites[48], which gradually disappeared on the surface of RuMo@MoOx-JH by shifting the potential negatively from OCV to −0.6 V (vs. RHE) (Fig. 6a). Nevertheless, the Raman band around *OH was basically remained on Mo@MoOx-JH under increasing potential (Fig. 6d). Meanwhile, the interfacial water structure was investigated from 3500 cm^{-1} to 4000 cm^{-1} and consisted of three distinct components (Fig. 6b, e), wherein the band located at 3627 cm^{-1} was characterized with weak hydrogen bonded water (named as free water). Other peaks could be assigned to O-H symmetric telescopic vibration (V_1(O-H):3858 cm^{-1}) and O-H anti-symmetric stretching vibration (V_3(O-H):3936 cm^{-1})[49]. It should be noted that the interfacial water with V_1(O-H) and V_3(O-H) tended to form rigid water network by hydrogen bonds and inhibited the transfer of OH species through interfacial water layer[50,51]. In fact, the Volmer step in alkaline HER involved easy-to-miss process of OH transfer process from electrode surface to bulk water: $*OH \rightarrow OH^- + *$, in which the high OH coverage might cause OH_{ad} poisoning effect to active sites thus limiting the HER performance[52]. Thus, the Gaussian fitting was performed for the interfacial water Raman signals and the relevant content was calculated in all potentials, as shown in Supplementary Fig. 42. Specifically, when the Ru was integrated with Mo after ultrafast Joule heating, the free water content was increased from average value of 26.4% to 36.5% compared with Mo@MoOx-JH (Fig. 6h). It has been reported that the asymmetrical atomic electric field could polarized water network due to the polar molecule structure[53], which effectively regulated the OH transfer process. To further confirm the speculation, the electronic structure was analyzed for the Mo NP and RuMo NA as shown in Fig. 6g. Different from the uniform charge density of Mo NP counterpart, the introduction of Ru caused distinctly regulated charge redistribution thus leading to asymmetrical field. Meanwhile, to improve the influence of water network by RuMo asymmetrical atomic electric field, the ab initio molecular dynamics (AIMD) simulation was performed (Supplementary Data 1), which was set at 300 K for 7 ps with time step 1 fs. The snapshots of interfacial water around electric field on surface at last step was shown in Fig. 6c, f. Interestingly, the interfacial water structure was rearranged around Ru, Mo sites, wherein the distance (2.575 Å) between water and metal was closer than that of pure Mo NP (2.834 Å), indicating accelerated H_2O adsorption process. Most importantly, the introduction of RuMo asymmetrical atomic electric field helped to weaken water network (Fig. 6i), which could be reflected by the decreased number of hydrogen bonds (30) and elongated bond length (2.39 Å) compared with Mo NP (35 and 2.37 Å). Referring the results obtained, we could confirm that the RuMo asymmetrical atomic electric field played an important role in regulated hydrogen bonds among interfacial water molecule, thus leading to accelerated OH transfer process and improved HER activity.

Highlight the role of Joule heating synthesis

Based on the aforementioned results, the introduction of RuMo NAs could effectively enhance the stability and activity of the catalyst for industrial current density. However, Ru-Mo system could be converted to alloys with ultra-high activation energy (≥1300 K), which was accompanied with atoms aggregation[22]. Consequently, to illustrate the superiority of rapid Joule heating, the temperature-programmed method was conducted for comparison (details in the Supporting information), wherein the in situ formation of Mo@MoOx and introducing of Ru were realized (denoted as Mo@MoOx-TG and RuMo-TG@MoOx-TG). Created by radiation heat through muffle furnace (Supplementary Fig. 43a), the local temperature among lumen was increased up to 973.15 K/1323.15 K with 5 K/min (Supplementary Fig. 43b, c), which could consume additional energy due to overall heating process of device (2500-folds of Joule heating). Specifically, the Ru-O-Mo species, during the thermal treatment, was transformed to thermodynamically driven aggregation with sheet morphology, which was completely covered onto NF (Supplementary Fig. 44). As could be seen from the CV curve and derived C_{dl} of RuMo-TG@MoOx-TG, the collapsed morphology played a negative role in the electrochemical active area (Supplementary Fig. 45a, b), wherein the C_{dl} value was 12.5 mF cm^{-2} and in sharp contrast to RuMo@MoOx-JH (389.6 mF cm^{-2}), indicating the excellent intrinsic activity endowed by rapid Joule heating. Meanwhile, the slow rising-cooling rate provided by temperature-programmed method enabled regressive surface wettability as evidenced by the significantly increased liquid contact angle from 0° (RuMo@MoOx-JH) to 129° (RuMo-TG@MoOx-TG), which might be the collapsed 3D arrays during the heating treatment[30] (Supplementary Fig. 45c). In addition, it was noteworthy that the prolonged temperature-programmed treatment deteriorated the charge transfer kinetics (Supplementary Fig. 45d, e), suggesting more tremendous potential for Joule heating. For comparison, the annealed

https://doi.org/10.1038/s41467-024-51976-5

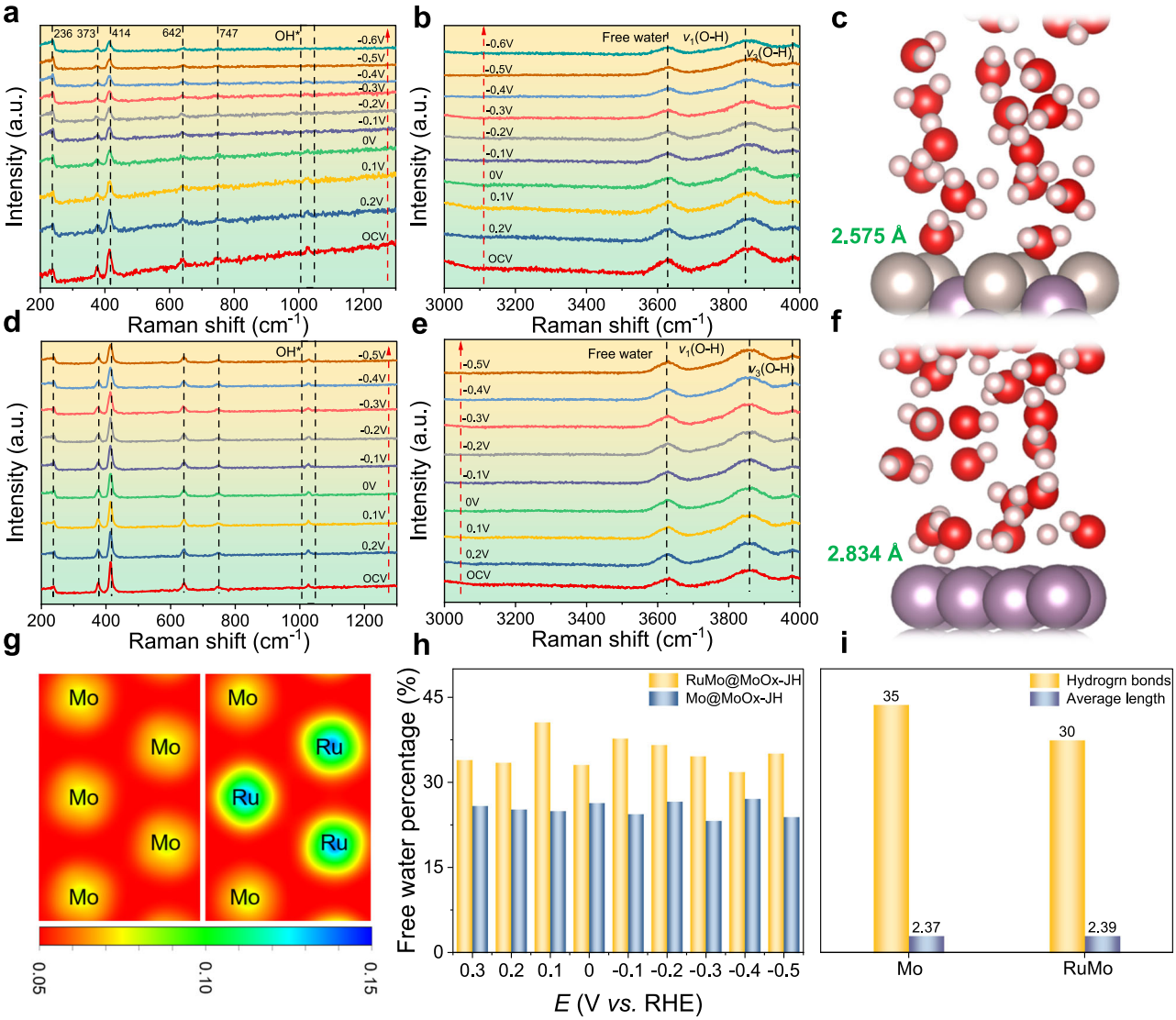

Fig. 6 | Insights of HER mechanism. a, **b** In-situ Raman spectra at RuMo@MoOx-JH surface. **c** Schematic of interfacial H_2O orientation of RuMo@MoOx-JH. **d**, **e** In-situ Raman spectra at Mo@MoOx-JH surface. **f** Schematic of interfacial H_2O orientation of Mo@MoOx-JH. **g** Charge density analyses of Mo@MoOx-JH (left) and RuMo@MoOx-JH (right). **h** The free water percentage along Mo@MoOx-JH and RuMo@MoOx-JH surfaces at different potentials. **i** Corresponding number of hydrogen bonds and average length. Source data for Fig. 6 are provided as a Source Data file.

RuMo-TG@MoOx-TG showed overpotential of 432 mV to deliver 500 mA cm^{-2}, which underwent severe HER performance decay (363% of RuMo@MoOx-JH: 119 mA @ 500 mA cm^{-2}) as shown in Supplementary Fig. 45f. As verification by the above results, the synthesized RuMo-TG@MoOx-TG, without modified by Joule heating, exhibited much deteriorated electrochemical properties than RuMo@MoOx-JH, indicating the efficiency of Joule heating for rational control of morphology and active sites.

To further investigate the impact of Joule heating on the MoOx support, the HER experiments of RuMo-JH@MoOx-TG were applied in 1 M KOH electrolyte (Fig. 7a), which was derived from Mo@MoOx-TG and further in situ treated on the Joule heating device same as RuMo@MoOx-JH (details in the Experimental Section). Specifically, the overpotential of RuMo-JH@MoOx-TG to deliver 50 mA cm^{-2} was 61 mV, which was 1.42 times higher than that of RuMo@MoOx-JH (43 mV). Considering the previous recognition of hydrogen spillover in Ru-based catalyst[54], which was highly correlated to the dioxide support properties. It could expect that the MoOx modified by rapid Joule heating played an important role in proton adsorption kinetics. Consequently, the *operando* EIS investigations was conducted on Mo@MoOx-JH, Mo@MoOx-TG, RuMo@MoOx-JH and RuMo-JH@MoOx-TG from the range of 0 mV to −140 mV (Supplementary Fig. 46). All the measured results could be simulated by double-parallel equivalent electric circuit (Supplementary Fig. 47) to investigate the protons accumulated behavior, which was consistent to the reported literatures[36,55]. The inner layer of electrode could be simulated by first parallel circuit consisted of resistor (denoted as R_{ct}) and constant phase element (denoted as CPE_2), indexing to charge transfer resistance and double-layer capacitance generated at low frequencies. Of note, the second parallel components were contributed to the electrolyte-catalyst interfacial hydrogen adsorption behavior, wherein the R_i and C_φ corresponded to hydrogen adsorption resistance and pseudo-capacitance among catalyst surface at high frequencies, respectively. Typically, the trend of EIS-derived Tafel slope plots was depicted as Fig. 7b and Supplementary Table 4, which was based on Ohm's law and related with hydrogen spillover[56]. Thus, it was rational to prove accelerated hydrogen spillover effect of RuMo@MoOx-JH due to the significantly reduced slope. Meanwhile, in terms of the integration of C_φ vs. potential profiles as shown in Fig. 7c, the adsorption amount of hydrogen (Q_H)

https://doi.org/10.1038/s41467-024-51976-5

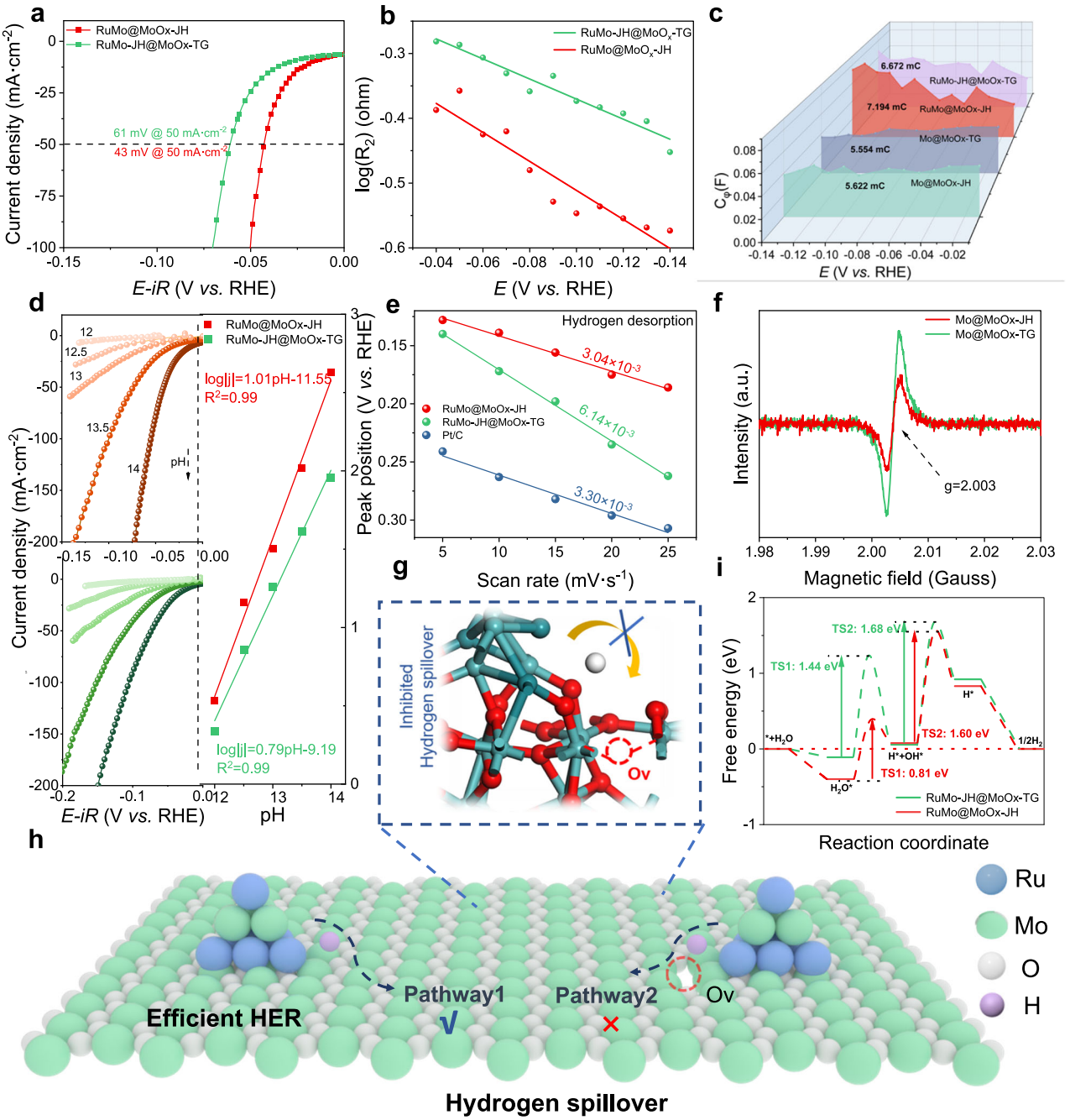

Fig. 7 | Insights of the role of Joule heating. a Polarization curves of RuMo@MoOx-JH with the reference of RuMo-JH@MoOx-TG (The electrode surface area was 1.0 cm × 1.0 cm, and the resistance was 1.60 ± 0.14 Ω). **b** EIS-derived Tafel plots of RuMo@MoOx-JH and RuMo-JH@MoOx-TG. **c** Plots of C_φ vs. potential. **d** Polarization curves of RuMo@MoOx-JH and RuMo-JH@MoOx-TG with various pH solutions and derived Tafel plots (The electrode surface area was 1.0 cm × 1.0 cm, and the resistance was provided in the Supplementary Information). **e** The linear plots of peak potentials vs. different scan rates. **f** Electron paramagnetic resonance spectra of Mo@MoOx-JH and Mo@MoOx-TG. **g**, **i** Proposed nature of hydrogen spillover phenomenon in RuMo@MoOx-JH and RuMo-JH@MoOx-TG. **h** Calculated free energy diagram for alkaline HER on RuMo@MoOx-JH and RuMo-JH@MoOx-TG. Source data for Fig. 7 are provided as a Source Data file.

during HER could be quantified (RuMo@MoOx-JH: 7.194 mC > RuMo-JH@MoOx-TG: 6.672 mC > Mo@MoOx-JH: 6.672 mC > Mo@MoOx-TG: 5.554 mC). The increased Q_H rationalized the enhanced pathway from RuMo NAs to MoOx. Besides, the hydrogen spillover mechanism was verified by reaction order based on pH-dependent environments from pH 12 to pH 14 (Fig. 7d). As tested, the experimental value of RuMo@MoOx-JH was determined to be 1.01, which was closer to theoretical 2.00 than that of RuMo-JH@MoOx-TG (0.79), indicating that the modified MoOx via Joule heating might be beneficial to the protons transfer[56]. Moreover, the hydrogen desorption kinetics was estimated from the dependence of hydrogen desorption peaks with various scan rates in the double layer region (Fig. 7e), which was derived from *operando* CV investigations (Supplementary Fig. 48). The desorption of underpotential deposited hydrogen (H_{upd}) on catalyst surface was crucial factor and were calculated to be 0.186 V at 25 mV s^{-1} for RuMo@MoOx-JH. The more negative value compared with RuMo-JH@MoOx-TG (0.262 V) and Pt/C (0.307 V) suggested weak hydrogen binding energy. Meanwhile, the slope order of RuMo@MoOx-JH (3.04×10^{-3}) < RuMo-JH@MoOx-TG (6.14×10^{-3}) < Pt/C (3.30×10^{-3}) undoubtably implied accelerated hydrogen

desorption kinetics endowed by rapid Joule heating and was consistent with hydrogen binding energy. Referring to previous study, such results was rational to be originated from the effectively hydrogen spillover effect[56]. The electron paramagnetic resonance spectra (EPR) was applied to investigate the hydrogen spillover from the difference in the microstructure for Mo@MoOx-JH and Mo@MoOx-TG as shown in Fig. 7f. It should be noted that the rapid Joule heating for Mo@MoOx-JH resulted in less formation of O_v among MoOx support, which might be caused by the ultrashort thermal reduction. In this case, the generated O_v could construct a Schottky junction and lead to intense interfacial charge accumulation, thus deriving kinetically spillover energy barrier from RuMo NAs to MoOx support[54] (Fig. 7g and i). The infer discussed above could be proved by the DFT calculations. In detail, the adsorption/dissociation behavior of H_2O were first investigated under alkaline conditions involving the reactive intermediates (*H_2O, *OH, *H). As shown in Fig. 7h, the calculated ΔG_{*H2O} of −0.40 eV for the RuMo@MoOx-JH model was evidently higher than −0.11 eV obtained from RuMo-JH@MoOx-TG model with O_v, indicating stronger adsorption strength of H_2O[16] (Supplementary Table 5). Furthermore, the water dissociation energy barrier for Ru site on RuMo@MoOx-JH presented as much lower value (0.81 eV) than that of RuMo-JH@MoOx-TG (1.44 eV) via heterolytic cleavage mode, indicating accelerated Volmer step[33]. On the support surface of RuMo@MoOx-JH and RuMo-JH@MoOx-TG, *H was adsorbed at final O site with ΔG_{*H} values of 0.83 eV and 0.92 eV, respectively, suggesting weak proton trapping, which functioned as hydrogen-poor "components" confirming possible protons transfer to O sites. The energy barrier for the channel of hydrogen spillover from RuMo NAs to MoOx was estimated, wherein the diffusion of H species across interface was hindered by existence of O_v (1.68 eV) compared with RuMo@MoOx-JH (1.60 eV) (Supplementary Table 5). In this term, such hydrogen spillover across the RuMo NAs to MoOx was significantly facilitated by rapid Joule heating, contributing to the enhanced HER activity.

Practical water splitting

To extend the practical application, the optimized RuMo@MoOx-JH was assigned as cathode among home-made anion exchange membrane alkaline water electrolyzer (AEM) with gas collection and recirculation devices. A counterpart AEM containing Pt/C (150 $\mu g_{Pt}/cm^{-2}$) was also investigated for comparison. As shown in Fig. 8a, Supplementary Figs. 49 and 50, as hydrogen were flushed out of chamber by KOH solution, the generated OH^- could flow through the anion exchange membrane (Supplementary Table 6) with losing of electrons and thus transformed to oxygen[57–60]. The polarization curves in Fig. 8b clearly revealed that the AEM based on RuMo@MoOx-JH||Ni foam owned improved water splitting performance compared with Pt/C||Ni foam, which required 2.63 V to deliver 1 A cm^{-2}. Of note, the RuMo@MoOx-JH||Ni foam system exhibited excellent water electrolysis activity (2.24 V@1 A cm^{-2}) even at 60 °C, which was much lower than that of Pt/C based electrolyzer (2.53 V@1 A cm^{-2}) suggesting the feasibility to practical application. Meanwhile, the developed AEM provided virtually unaffected performance compared with Pt/C||Ni foam under high flow rates (Supplementary Figs. 51 and 52), which was originated from effective gas escape among three-phase contact area (solid-liquid-gas) due to the optimal RuMo@MoOx-JH[22]. As further evidenced by liquid contact angles test in Supplementary Fig. 53, the significant decreased contact angle for RuMo@MoOx-JH (0°) substantiated the remarkable surface wettability compared to the Pt/C (129°) thus favoring the electrolyte-catalyst contact surface. Meanwhile, the polarization curves of the RuMo@MoOx-JH||Ni foam system in the ultra-pure water and 1 M PBS electrolyte was shown in Supplementary Fig. 54, which could obtain 150 mA cm^{-2} at 4.02 V and 1000 mA cm^{-2} at 2.95 V, respectively.

Besides, the alkaline AEM electrolyzer catalyzed by different anodes, including NiFe-LDH, commercial IrO_2, and NF, were further assembled as shown in Fig. 8c, Supplementary Figs. 55 and 56. It should be noted that the RuMo@MoOx-JH||NiFe- LDH and RuMo@MoOx-JH||IrO_2 exhibited excellent polarization property, with a low cell voltage of only 1.73 V and 1.84 V to achieve a high current density of 1 A cm^{-2} at 60 °C in the KOH electrolyte, respectively. Considering the excellent performance, the following discussion was based on the RuMo@MoOx-JH||NiFe-LDH system. The energy consumption per cubic meter of hydrogen was another essential standard for investigating practical potential, which inhibited the efficiency of commercial alkaline water splitting (energy consumption ranged from 4.5 to 5.1 kW h)[61]; we thus evaluated the RuMo@MoOx-JH||NiFe LDH (2 cm × 2 cm) electrolyzer as shown in Fig. 8d, e. It far surpassed the current level of commercial AEM, which required 4.11 kW h m^{-3} at 300 mA cm^{-2} with ~100% Faradic efficiency (Supplementary Fig. 57). Meanwhile, such AEM-based electrolyzer exhibited excellent stability at 1000 mA cm^{-2} in KOH solution (Supplementary Fig. 58). Meanwhile, under the temperature of 40 °C and 60 °C, such electrolyzer rendered an impressive optimum energy consumption benefit with 3.86 kW h m^{-3} and 3.82 kW h m^{-3} at 300 mA cm^{-2}, respectively (Fig. 8e). Moreover, consistent with unit electricity consumption per cubic meter hydrogen, the electricity-to-hydrogen energy conversion efficiency (η_{ETH}) was calculated to be 81.5%, 86.5% and 89.2% at 20 °C, 40 °C and 60 °C, respectively[61] (Supplementary Fig. 59). Furthermore, to evaluated the feasibility for large-scale synthesis, the price of RuMo@MoOx-JH was found to be 90.85 US $ m^{-2} based on the Supplementary Table 7, which was 100 times lower than that of commercial Pt/C electrode (~9100 US$ m^{-2}) even closed to commercial raney Ni (~60 US$ m^{-2}). The above results clearly confirmed the superior performance for future industrial application.

In summary, we proposed a Joule heating method by alloying Ru and Mo on MoOx matrix to construct RuMo@MoOx-JH catalyst towards HER. As-synthesized RuMo@MoOx-JH catalyst exhibited a stable operation of >2000 h among 1 A cm^{-2} in KOH solution without obvious decay, wherein Mo migration following introduction of Ru was restrained by increased vacancy formation energy (9.36 eV) and raised Mo-O* antibonding energy level. Meanwhile, benefited by introduced asymmetric electric field by RuMo NAs, the interfacial water network was regulated (hydrogen bonds: 35 to 30; bond length 2.37 Å to 2.39 Å), leading to accelerated OH transfer process as evidenced by in situ Raman measurement and molecular dynamics. As expected, RuMo@MoOx-JH exhibited low overpotentials of 9 mV, 169 mV, and 256 mV to achieve 10, 1000, and 2000 mA cm^{-2} in KOH solution and even showed pH-universal activity in 1 M PBS (18 mV @ 10 mA cm^{-2}) and 0.5 M H_2SO_4 (15 mV @ 10 mA cm^{-2}). Furthermore, experimental and DFT results suggested the significant role of rapid Joule heating in enhancing electrocatalytic performance. Finally, AEM water electrolyzer was resembled with the introduction of RuMo@MoOx-JH, which exhibited excellent operating performance (electricity consumption: 3.82 kW h m^{-3} @ 300 mA cm^{-2} and electricity-to-hydrogen energy conversion efficiency: 89.2% at 60 °C).Such excellent performance was investigated in electronic structure and catalyst-electrolyte interactions level, which not only provided feasible method and understanding to synthesize high active and robust alloy-based cathode but also allowed implementation in AEM for industrial-level water splitting.

Methods

Catalyst synthesis

The RuMo@MoOx-JH was synthesized by two-step Joule heating method. Firstly, a pre-cleaned piece of NF (3 cm × 4 cm × 1 mm) was immersed in the solution of 4.0 mmol ammonium molybdate tetrahydrate, which was dissolved in 75.0 ml ultrapure water, followed by ultrasonication for 30 min. The above solution with NF was transferred to a 90-mL Teflon-lined autoclave and heated at 150 °C for 6 h to obtain MoO_3. Then, a piece of MoO_3 (1 cm × 1.5 cm × 1 mm) was rapidly heated

https://doi.org/10.1038/s41467-024-51976-5

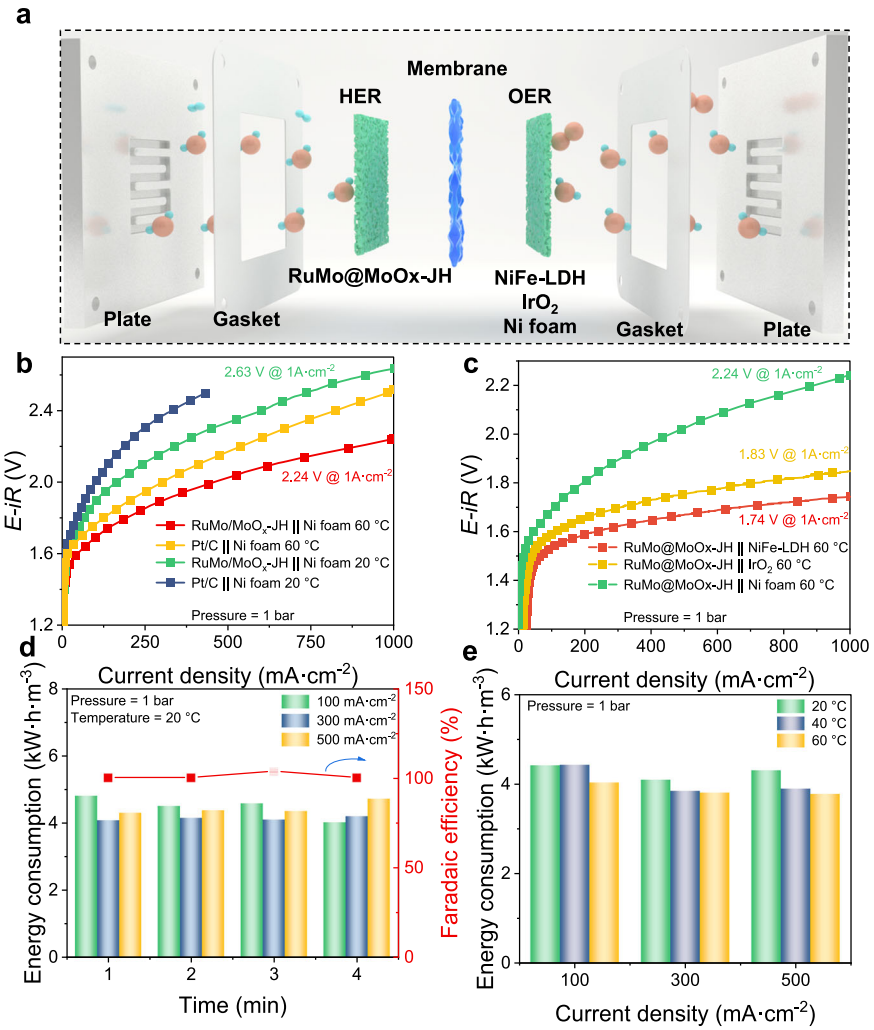

Fig. 8 | AEM device performance based RuMo@MoOx-JH as cathode. **a** Schematic diagram of the AEM device with symmetric alkaline water supply. **b** Polarization curves of AEM using RuMo@MoOx-JH or commercial Pt/C as cathode and Ni foam as anode at different temperatures and ambient pressure (The electrode surface area was 0.5 cm × 0.4 cm, and the resistance was 0.96 ± 0.17 Ω at 60 °C; 2.11 ± 0.57 Ω at 20 °C). **c** Polarization curves of AEM with different anodes (The electrode surface area was 0.5 cm × 0.4 cm, and the resistance was 0.97 ± 0.10 Ω). **d** Consumed electricity energy of RuMo@MoOx-JH || NiFe LDH for different current density at 20 °C and ambient pressure, wherein the faradic efficiency was measured at 300 mA cm^{-2}. **e** Consumed electricity energy of RuMo@MoOx-JH || NiFe LDH for different current density and temperature. Source data for Fig. 8 are provided as a Source Data file.

at 973.1 K through Joule heating method (Hefei in situ technology Co., Ltd. China) for 60 s in Ar-H_2 (10 %) flow with ramp up rate of 84.4 K s^{-1} and cool down rate of 361.0 K s^{-1} to obtain MoOx-JH. Finally, a piece of Mo@MoOx-JH (1 cm × 1.5 cm) was immersed in Ruthenium (III) chloride solution for 2 min, and taken out and dried in an infrared desiccator. The obtained sample was then heated at 1303.1 K with Joule heating method to achieve RuMo@MoOx-JH, while furnishes ramp up rate of 2010.0 K s^{-1}. The mass loading of RuMo@MoOx-JH on NF was measured to be 3.78 mg cm^{-2}, wherein the mass loading of Ru elements was 136 μg cm^{-2}. The mass loading of other controls was identical to RuMo@MoOx-JH.

Characterizations

XRD measurements were employed on D8 Advance using Cu Kα radiation with scan rate 10° min^{-1}. Scanning electron microscopy (SEM) images were performed on TESCAN MIRA LMS microscope operated at an acceleration voltage of 5–10 kV. X-ray photoelectron spectroscopy (XPS) measurements were carried out on Thermo Scientific ESCALAB Xi+ at 0.0108 A and 14795.40 V using a monochromatic Al Kα source. The spectra were analyzed using Avantage software. Transmission electron microscopy (TEM) was performed on FEI Tecnai G2F 20 microscope, wherein line-scanning profile across the RuMo NAs was obtained via energy dispersive spectrometry (EDS-mapping, JEM-F200). The TEM samples were prepared by detaching the catalyst from the NF substrates through a gentle sonication. Inductively Coupled Plasma-Optical Emission Spectrometer (ICP-OES) measurements were recorded on a Thermo Fisher iCAP PRO (OES). Depending on the requirements, the samples were prepared by collecting electrolyte after the water splitting. Electron Paramagnetic Resonance (EPR) experiment was conducted on a Bruker A300-10/12. A Dataphysics OCA 20 contact angle system was employed to measure the hydrophilicity of the electrodes. X-ray absorption near-edge structure (XANES) and extended X-ray absorption fine structure (EXAFS) were carried out with Si (111) crystal monochromators at the BL14W beamline at the Shanghai Synchrotron Radiation S7 Facility (SSRF, BL14W1 station, operated at 3.5 GeV with a maximum current of 250 mA) (Shanghai, China). For the in situ Raman measurement, the Raman spectroscopic measurements were performed using a SmartRaman confocal micro-Raman module (Institute of Semiconductors, Chinese Academy of Sciences) with 532 nm laser. Measurements were conducted with ×50 objective lens, which was detected with a Horiba iHR550 spectrometer and an optical charge-coupled device (CCD).

Electrochemical measurements

All the electrocatalytic tests were carried out on CHI electrochemical analyzer (CH Instruments Ins.) with conventional three-electrode configuration at 25 °C. The HER/OER tests were conducted in H_2/O_2-saturated solutions to ensure the equilibrium potential of water oxidation reaction. The CHI 680D high current amplifier was equipped with CHI 660E electrochemical analyzer, which was applied to the situation where the current is out of range. During the electrochemical measurements, the catalysts on NF, Hg/HgO (Hg/Hg_2Cl_2 and Hg/Hg_2SO_4) electrode, and the winded Pt wire were used as the working, reference, and counter electrodes, respectively. Note: during the test, the carbon rod was not applied as counter electrode due to the release of carbon ash under high working current density. The area of the electrode applied in the electrochemical analysis was 0.5 cm × 0.4 cm for electrochemical analysis. Meanwhile, to confirm the reproducibility of results, the HER performance of RuMo@MoOx-JH was reassessed at low current density, wherein the active area was 1.0 cm × 1.0 cm on NF and 0.07065 cm^2 on glassy carbon electrode. 1 M KOH/ 0.5 M H_2SO_4/ 1 M PBS solution was used as the electrolyte solution. Linear sweep voltammetry (LSV) was measured at a scan rate of 5 mV s^{-1} and was 100% *iR*-corrected in our work (i was the real working current and R is the measured series resistance). Meanwhile, the resistance for the *iR*-compensation was obtained at the open circuit potential of electrochemical cell. The electrochemical impedance spectroscopy (EIS) measurements were applied at different potentials, wherein the frequency ranged from 10^5 to 10^{-3} Hz. The Faradaic efficiency of the RuMo@MoOx-JH was calculated by measuring the amount of evolved H_2 through water drainage method at 300 mA cm^{-2}, which was as follows:

$$\text{Faradaic efficiency} = N_G/N_T \quad (1)$$

$$N_G = V/V_m \quad (2)$$

$$N_T = Q/(2 \times F) \quad (3)$$

where N_G is the number of generated hydrogen molecules; N_T is the theoretical number of hydrogen molecules; V is the measured volume of hydrogen; V_m is molar volume of gas; Q indicated the number of electrons transferred to generate hydrogen.

Data availability

The authors declare that the data supporting the findings of this study are available within the paper and its Supplementary Information files. The Source data are provided with this paper. Should any raw data files be needed in another format they are available from the corresponding author upon request. Source data are provided with this paper.

References

1. Wang, X. et al. Developing a class of dual atom materials for multifunctional catalytic reactions. *Nat. Commun.* **14**, 7210–7223 (2023).
2. Zuo, Y. et al. Ru-Cu nanoheterostructures for efficient hydrogen evolution reaction in alkaline water electrolyzers. *J. Am. Chem. Soc.* **145**, 21419–21431 (2023).
3. Bartels, J. R., Pate, M. B. & Olson, N. K. An economic survey of hydrogen production from conventional and alternative energy sources. *Int J. Hydrog. Energ.* **35**, 8371–8384 (2010).
4. Du, W., Shi, Y., Zhou, W., Yu, Y. & Zhang, B. Unveiling the in situ dissolution and polymerization of Mo in Ni_4Mo alloy for promoting the hydrogen evolution reaction. *Angew. Chem. Int Ed. Engl.* **60**, 7051–7055 (2021).
5. Zhao, Z., Sun, J., Li, X., Zhang, Z. & Meng, X. Joule heating synthesis of NiFe alloy/MoO_2 and in-situ transformed (Ni,Fe)OOH/MoO_2 heterostructure as effective complementary electrocatalysts for overall splitting in alkaline seawater. *Appl Catal. B Environ.* **340**, 123277–123294 (2024).
6. Zhang, J. et al. Efficient hydrogen production on $MoNi_4$ electrocatalysts with fast water dissociation kinetics. *Nat. Commun.* **8**, 15437–15445 (2017).
7. Xiong, G. et al. Rapid synthesis of various electrocatalysts on Ni foam using a universal and facile induction heating method for efficient water splitting. *Adv. Funct. Mater.* **31**, 2009580–2009591 (2021).
8. Zhai, P. et al. Engineering active sites on hierarchical transition bimetal oxides/sulfides heterostructure array enabling robust overall water splitting. *Nat. Commun.* **11**, 5462–5474 (2020).
9. Du, W., Shi, Y., Zhou, W., Yu, Y. & Zhang, B. Unveiling the in situ dissolution and polymerization of Mo in Ni(4) Mo alloy for promoting the hydrogen evolution reaction. *Angew. Chem. Int Ed. Engl.* **60**, 7051–7055 (2021).
10. Gao, L. et al. Unconventional p-d hybridization interaction in PtGa ultrathin nanowires boosts oxygen reduction electrocatalysis. *J. Am. Chem. Soc.* **141**, 18083–18090 (2019).
11. He, C. et al. Low-Iridium-Content $IrIn_2$ intermetallics with an unconventional face-centered orthorhombic phase for efficient overall water splitting. *Adv. Funct. Mater.* **34**, 2311683–2311692 (2023).
12. Zhao, X. et al. A double atomic-tuned RuBi SAA/Bi@OG nanostructure with optimum charge redistribution for efficient hydrogen evolution. *Angew. Chem. Int Ed. Engl.* **62**, e202300879 (2023).
13. Kuang, P., Ni, Z., Zhu, B., Lin, Y. & Yu, J. Modulating the d-band center enables ultrafine Pt_3Fe alloy nanoparticles for pH-universal hydrogen evolution reaction. *Adv. Mater.* **35**, 2303030–2303041 (2023).
14. Escudero-Escribano, M. et al. Tuning the activity of Pt alloy electrocatalysts by means of the lanthanide contraction. *Science* **352**, 73-76 (2016).
15. Greeley, J. et al. Alloys of platinum and early transition metals as oxygen reduction electrocatalysts. *Nat. Chem.* **1**, 552–556 (2009).
16. Xiao, X., Li, Z., Xiong, Y. & Yang, Y. W. IrMo nanocluster-doped porous carbon electrocatalysts derived from cucurbit[6]uril boost efficient alkaline hydrogen evolution. *J. Am. Chem. Soc.* **145**, 16548–16556 (2023).
17. Tu, K. et al. A novel heterostructure based on RuMo nanoalloys and N-doped carbon as an efficient electrocatalyst for the hydrogen evolution reaction. *Adv. Mater.* **32**, 2005433–2005443 (2020).
18. Pang, B. et al. Laser-assisted high-performance PtRu alloy for pH-universal hydrogen evolution. *Energy Environ. Sci.* **15**, 102–108 (2022).
19. Elbert, K. et al. Elucidating hydrogen oxidation/evolution kinetics in base and acid by enhanced activities at the optimized Pt shell thickness on the Ru core. *ACS Catal.* **5**, 6764–6772 (2015).
20. Jakšić, M. J. E. A. Electrocatalysis of hydrogen evolution in the light of the brewer—engel theory for bonding in metals and intermetallic phases. *Electrochim. Acta* **29**, 1539–1550 (1984).
21. Hernandez-Fernandez, P. et al. Mass-selected nanoparticles of PtxY as model catalysts for oxygen electroreduction. *Nat. Chem.* **6**, 732–738 (2014).
22. Yuan, H. et al. Laser synthesis of PtMo single-atom alloy electrode for ultralow voltage hydrogen generation. *Adv. Mater.* **36**, 2305375–2305385 (2023).
23. Wulan, B., Cao, X., Tan, D., Ma, J. & Zhang, J. To stabilize oxygen on In/In_2O_3 heterostructure via joule heating for efficient electrocatalytic CO_2 reduction. *Adv. Funct. Mater.* **33**, 2209114–2209123 (2022).
24. Sun, J. et al. Joule heating synthesis of well lattice-matched $Co_2Mo_3O_8/MoO_2$ heterointerfaces with greatly improved hydrogen

evolution reaction in alkaline seawater electrolysis with 12.4 % STH efficiency. *Appl. Catal. B Environ.* **338**, 123015–123026 (2023).
25. Yu, F. et al. Rapid self-heating synthesis of Fe-based nanomaterial catalyst for advanced oxidation. *Nat. Commun.* **14**, 4975–4985 (2023).
26. Wagman, D. D. et al. The NBS tables of chemical thermodynamic properties. Selected values for inorganic and C1 and C2 organic substances in SI units. *J. Phys. Chem. Ref. Data* **18**, 1807–1812 (1982).
27. Chase, M. Jr et al. JANAF thermochemical tables: II: Cr-Zr. *J. Phys. Chem. Ref. Data* **14**, 927–1856 (1985).
28. Cox, J. D., Wagman, D. D. & Medvedev, V. A. J. CODATA key values for thermodynamics. (1989).
29. Yan, W. et al. PCTS-controlled synthesis of L10/L12-typed Pt-Mn intermetallics for electrocatalytic oxygen reduction. *Adv. Funct. Mater.* **34**, 2310487–2310497 (2023).
30. Dou, S. et al. High-temperature shock enabled nanomanufacturing for energy-related applications. *Adv. Energy Mater.* **10**, 2001331–2001346 (2020).
31. Li, Y. et al. The evolution of dislocation loop and its interaction with pre-existing dislocation in He+-irradiated molybdenum: in-situ TEM observation and molecular dynamics simulation. *Acta Mater.* **201**, 462–476 (2020).
32. Liu, P. et al. Frank partial dislocations in coplanar Ir/C ultrathin nanosheets boost hydrogen evolution reaction. *Adv. Mater.* **36**, 2310591–2310599 (2023).
33. Cao, D., Xu, H. & Cheng, D. Construction of defect-rich RhCu nanotubes with highly active Rh_3Cu_1 alloy phase for overall water splitting in all pH values. *Adv. Energy Mater.* **10**, 1903038–1903050 (2020).
34. Zhang, Y. et al. Hetero-interface manipulation in MoOx@Ru to evoke industrial hydrogen production performance with current density of 4000 mA cm^{-2}. *Adv. Energy Mater.* **13**, 2301492–2301502 (2023).
35. Huang, C., Zhang, W. & Zheng, W. The debut and spreading the landscape for excellent vacancies-promoted electrochemical energy storage of nano-architected molybdenum oxides. *Mater. Today Energy* **30**, 101154–101174 (2022).
36. Chen, J. et al. Reversible hydrogen spillover in Ru-WO_{3-x} enhances hydrogen evolution activity in neutral pH water splitting. *Nat. Commun.* **13**, 5382–5392 (2022).
37. Lin, G. et al. Caged-cation-induced lattice distortion in bronze TiO_2 for cohering nanoparticulate hydrogen evolution electrocatalysts. *ACS nano* **16**, 9920–9928 (2022).
38. Zeng, B. et al. Grafting ultra-fine nanoalloys with amorphous skin enables highly active and long-lived acidic hydrogen production. *Angew. Chem. Int. Ed. Engl.* **63**, e202400582 (2024).
39. Jiang, B. et al. Noble-metal-metalloid alloy architectures: mesoporous amorphous iridium-tellurium alloy for electrochemical N_2 reduction. *J. Am. Chem. Soc.* **145**, 6079–6086 (2023).
40. Jiang, Z. et al. Lattice strain and schottky junction dual regulation boosts ultrafine ruthenium nanoparticles anchored on a N-Modified carbon catalyst for H_2 production. *J. Am. Chem. Soc.* **144**, 19619–19626 (2022).
41. Wu, D. et al. Efficient overall water splitting in acid with anisotropic metal nanosheets. *Nat. Commun.* **12**, 1145–1154 (2021).
42. Chen, W. et al. Deciphering the alternating synergy between interlayer Pt single-atom and NiFe layered double hydroxide for overall water splitting. *Energy Environ. Sci.* **14**, 6428–6440 (2021).
43. Zhou, L. et al. Stabilizing non-iridium active sites by non-stoichiometric oxide for acidic water oxidation at high current density. *Nat. Commun.* **14**, 7644–7656 (2023).
44. Cao, J. et al. Improved electrocatalytic activity and stability by single iridium atoms on iron-based layered double hydroxides for oxygen evolution. *Angew. Chem. Int Ed. Engl.* **62**, e202310973 (2023).
45. Li, C. et al. Ultrafast self-heating synthesis of robust heterogeneous nanocarbides for high current density hydrogen evolution reaction. *Nat. Commun.* **13**, 3338–3349 (2022).
46. Liu, J. et al. Optimizing hydrogen adsorption by d–d orbital modulation for efficient hydrogen evolution catalysis. *Adv. Energy Mater.* **12**, 2103301–2103310 (2022).
47. Liu, P. et al. NiMoFe nanoparticles@MoO_2 nano-pillar arrays as bifunctional electrodes for ultra-low-voltage overall water splitting. *J. Mater. Chem. A* **10**, 3760–3770 (2022).
48. Zhang, Z. et al. Metal–organic framework-derived hollow nanocubes as stable noble metal-free electrocatalyst for water splitting at high current density. *CCS Chem.* **6**, 1324–1337 (2023).
49. Wang, S.-H., Li, Z.-L., Sun, C.-L., Li, Z.-W. & Men, Z.-W. Influence of laser-induced plasma on stimulated Raman scatting of OH stretching vibrational from water molecules. *Acta Phys. Sin.* **63**, 205204–205209 (2014).
50. Deng, Y. & Yeo, B. S. Characterization of electrocatalytic water splitting and CO_2 reduction reactions using in situ/operando raman spectroscopy. *ACS Catal.* **7**, 7873–7889 (2017).
51. Wang, M. et al. Interfacial water activation by single-atom Co–N_3 sites coupled with encapsulated Co nanocrystals for accelerating electrocatalytic hydrogen evolution. *ACS Catal.* **12**, 10771–10780 (2022).
52. Zhang, J. et al. Competitive adsorption: reducing the poisoning effect of adsorbed hydroxyl on Ru single-atom site with SnO_2 for efficient hydrogen evolution. *Angew. Chem. Int Ed. Engl.* **61**, e202209486 (2022).
53. Cai, C. et al. Atomically local electric field induced interface water reorientation for alkaline hydrogen evolution reaction. *Angew. Chem. Int Ed. Engl.* **62**, e202300873 (2023).
54. Li, J. et al. A fundamental viewpoint on the hydrogen spillover phenomenon of electrocatalytic hydrogen evolution. *Nat. Commun.* **12**, 3502–3514 (2021).
55. Zhou, S. et al. Boosting hydrogen evolution reaction by phase engineering and phosphorus doping on Ru/P-TiO(2). *Angew. Chem. Int Ed. Engl.* **61**, e202212196 (2022).
56. Dai, J. et al. Hydrogen spillover in complex oxide multifunctional sites improves acidic hydrogen evolution electrocatalysis. *Nat. Commun.* **13**, 1189–1199 (2022).
57. Thangavel, P. et al. Graphene-nanoplatelets-supported NiFe-MOF: high-efficiency and ultra-stable oxygen electrodes for sustained alkaline anion exchange membrane water electrolysis. *Energy Environ. Sci.* **13**, 3447–3458 (2020).
58. Thangavel, P., Kim, G. & Kim, K. S. Electrochemical integration of amorphous NiFe (oxy)hydroxides on surface-activated carbon fibers for high-efficiency oxygen evolution in alkaline anion exchange membrane water electrolysis. *J. Mater. Chem. A* **9**, 14043–14051 (2021).
59. Kong, T.-H. et al. In-situ ionomer-free catalyst-coated membranes for anion exchange membrane water electrolyzers. *ACS Energy Lett.* **8**, 4666–4673 (2023).
60. Thangavel, P. et al. Immobilizing low-cost metal nitrides in electrochemically reconstructed platinum group metal (PGM)-free oxy-(hydroxides) surface for exceptional OER kinetics in anion exchange membrane water electrolysis. *Adv. Energy Mater.* **13**, 2203401–2203410 (2023).
61. Fang, P. et al. Making ternary-metal hydroxysulfide catalyst via cathodic reconstruction with ion regulation for industrial-level hydrogen generation. *Adv. Energy Mater.* **13**, 2301222–2301233 (2023).

Acknowledgements

This work was financially supported by Taishan Scholars Foundation of Shandong province (No.: tsqn201909058), Shandong Provincial Natural Science Foundation (No.: ZR2021QB056), and the Fundamental

Research Funds for the Central Universities (No: 202441006, 202364004, and 202461025).

Author contributions

Xiangchao Meng and Zhan Zhao conceived the idea, designed the electrochemical experiments, and revised the manuscript. Zhan Zhao, Zisheng Zhang, and Shiyu Qin contributed to the DFT calculations. Jianpeng Sun and Xiang Li assisted in electrochemical experiments and characterizations for materials. Xiangchao Meng, Chunhu Li, and Zizhen Li contributed to the structural and electrochemical analysis and final version of the manuscript.

Competing interests

The authors declare no competing interests.

Additional information

Supplementary information The online version contains supplementary material available at https://doi.org/10.1038/s41467-024-51976-5.

Correspondence and requests for materials should be addressed to Xiangchao Meng.

Peer review information *Nature Communications* thanks the anonymous reviewers for their contribution to the peer review of this work. A peer review file is available.